

Observation of quantum oscillations, linear magnetoresistance, and crystalline electric field effect in quasi-two-dimensional PrAgBi₂

Sudip Malick,^{1,2,*} Hanna Świątek,^{1,2} Michał J Winiarski,^{1,2,†} and Tomasz Klimczuk^{1,2,‡}

¹*Faculty of Applied Physics and Mathematics, Gdansk University of Technology, Narutowicza 11/12, 80-233 Gdańsk, Poland*

²*Advanced Materials Center, Gdansk University of Technology, Narutowicza 11/12, 80-233 Gdańsk, Poland*

We report the magnetic and magnetotransport properties with electronic band structure calculation of the Bi square net system PrAgBi₂. The magnetization and heat capacity data confirm the presence of a crystalline electric field (CEF) effect in PrAgBi₂. Analysis of the CEF effect using a multilevel energy scheme reveals that the ground state of PrAgBi₂ consists of five singlets and two doublets. The de Haas-van Alphen (dHvA) quantum oscillations data show a single frequency with a very small cyclotron effective mass of approximately 0.11 m_e . A nontrivial Berry phase is also observed from the quantum oscillations data. The magnetotransport data shows linear and unsaturated magnetoresistance, reaching up to 1060% at 2 K and 9 T. Notably, there is a crossover from a weak-field quadratic dependence to a high-field linear dependence in the field-dependent magnetoresistance data. The crossover critical field B^* follows the quadratic temperature dependence, indicating the existence of Dirac fermions. The band structure calculation shows several Dirac-like linear band dispersion near the Fermi level and a Dirac point close to the Fermi level, located at the Brillouin zone boundary. *Ab initio* calculations allowed us to ascribe the observed dHvA oscillation frequency to a particular feature of the Fermi surface. Our study suggests layered PrAgBi₂ is a plausible candidate for hosting the CEF effect and Dirac fermion in the Bi square net.

I. INTRODUCTION

Recently, quasi-two-dimensional (2D) pnictides have been receiving significant attention as they appear to host relativistic fermions. Such fermions are generated in these systems when two $p_{x,y}$ bands from Bi/Sb intersect and form linear energy dispersion, resulting in Dirac and Weyl states. Since electron transport in these compounds is driven by relativistic fermions, several quantum phenomena emerge, including linear magnetoresistance (MR), quantum oscillations, quantum Hall effect, large mobility, superconductivity and anisotropic transport properties [1–10]. Consequently, these quantum materials show great potential for unique physical properties and practical applications.

AMnSb₂ and AMnBi₂ ($A = \text{Ca, Sr, Ba, and Eu}$) are a well-studied series with quasi-2D structures containing Bi/Sb square sheets [11–24]. It was found that these compounds crystallize mainly in tetragonal and orthorhombic structures. The different A ions may lead to the formation of different crystal structures. (Ca/Sr)MnSb₂ crystallizes in the $Pnma$ space group [11, 13], whereas CaMnBi₂ takes the $P4/nmm$ space group [5]; it changes to $I4/mmm$ in the case of (Sr/Ba/Eu)MnBi₂ [6, 22, 24]. Several measurements, such as electron transport, angle-resolved photoemission spectroscopy (ARPES) and first-principles calculations, confirm the existence of Dirac fermions in the Bi/Sb square nets [1, 25, 26]. Some compounds show magnetism, breaking the time-reversal symmetry and leading to Weyl states. The physical properties of rare-earth (R) silver bismuthide and antimonide

RAgBi₂ and RAgSb₂, which belong to the same family, were investigated a few decades ago [27, 28]. Most compounds in this family exhibit long-range antiferromagnetic ordering competing with crystalline electric field (CEF) effect at low temperatures. As an exception, the ground state of PrAgBi₂ was assumed to be non-magnetic, pending further investigations [27]. These compounds have recently gained attention since they have been categorized as potential hosts for Dirac fermions. Linear MR has been observed in LaAgBi₂ and LaAgSb₂, which is ascribed to the quantum limit of the possible Dirac fermions [29, 30]. ARPES data suggest the existence of a Dirac cone in LaAgSb₂ along the Γ - M high-symmetry line [31]. Anisotropic electron transport and high mobility are observed in antiferromagnetic GdAgSb₂ [32] and SmAgSb₂ [33]. Quantum oscillations study indicates a topological phase transition from non-trivial to trivial states as the system moves away from the antiferromagnetic states in SmAgSb₂ [33].

In this paper, we have grown high-quality single crystals of rare earth silver dibismuthide PrAgBi₂ and carried out a detailed analysis of the magnetic, thermodynamic, and magnetotransport data in conjunction with the band structure calculations. The magnetization and heat capacity data analyses confirm the presence of the CEF effect in PrAgBi₂. The de Haas-van Alphen (dHvA) oscillations data reveal a very low cyclotron effective mass and a nonzero Berry phase, which are consistent with the Dirac-like band dispersion observed in the band structure calculation. Additionally, magnetotransport data exhibits large unsaturated linear MR and a crossover from quadratic to linear field dependence. The Hall resistivity data suggest the presence of two types of carriers in PrAgBi₂. The paper is organized as follows: The method of crystal growth, measurements, and band structure calculation is presented in Sec. II. The crystal structure of

* sudip.malick@pg.edu.pl

† michal.winiarski@pg.edu.pl

‡ tomasz.klimczuk@pg.edu.pl

PrAgBi₂ is briefly discussed in Sec. III A. Analysis of the CEF effect and dHvA oscillations is demonstrated in Sec. III B and Sec. III C, respectively. Sec. III D and Sec. III E discuss the magnetoresistance and Hall resistivity data, respectively. The band structure of PrAgBi₂ is presented in Sec. III F. Finally, we conclude our results in Sec. IV.

II. METHODS

High quality single crystals of PrAgBi₂ and LaAgBi₂ were grown via self-flux method, using pieces of high purity Pr/La (99.9%), Ag (99.99%) and Bi (99.99%) in a 1:1:10 ratio. The alumina crucible containing the elements was sealed in an evacuated, partially argon back-filled quartz tube. It was then heated to 1000°C and held there for 12 h, followed by slow cooling at the rate of 3°C/h. The tube was taken out of the furnace at 500°C and centrifuged to separate the crystals from the flux. The crystal structure was determined by x-ray diffraction (XRD) using a Bruker D2 Phaser diffractometer with Cu K α radiation and a LynxEye XE-T detector. Physical properties were investigated using a Quantum Design Physical Property Measurement System with a vibrating sample magnetometer attachment for the magnetic measurements. The resistivity measurement employed a standard four probe technique with an applied current of 5 mA. Heat capacity was measured using a two- τ relaxation method. Electronic structure calculations were performed by means of the plane-wave basis Density Functional Theory (DFT) using the Quantum Espresso 7.2 package [34–36], employing the Perdew-Burke-Ernzerhof Generalized Gradient Approximation (PBE GGA) [37] of the exchange-correlation potential and the Projector-Augmented Wave (PAW) [38] method in a fully-relativistic (spin-orbit coupling included) mode. Suitable PAW sets were taken from the PSLibrary [39]. The $4f$ orbitals of Pr were treated as core states. The unit cell and structural parameters were relaxed using the Broyden-Fletcher-Goldfarb-Shanno (BFGS) to method yielding $a = 4.618$ Å, $c = 10.444$ Å, Pr position (0, 0.5, 0.74839), Bi1 position (0, 0.5, 0.18396), with all other atomic parameters fixed by symmetry. Self-consistent calculations were completed on a $12 \times 12 \times 5$ k -point mesh with density and plane-wave cutoff energies set to 500 and 50 Ry, respectively. Fermi surface (FS) images were rendered using the FermiSurfer 2.4.0 program [40] The SKEAF program [41] was used to calculate the dHVA oscillation frequencies for each of the FS branches. In order to obtain a sufficiently dense k -point grid, the FS file for SKEAF was calculated using an all-electron full potential linearized augmented plane wave (FP-LAPW) DFT code ELK 10.0.15, employing the PBE GGA. The correlation effects in the $4f$ shell of Pr was treated using the DFT+U formalism in the fully-localized limit. The Hubbard U and exchange J parameters were set to 6.5 eV and 1.1 eV, respectively. The structural relaxation and

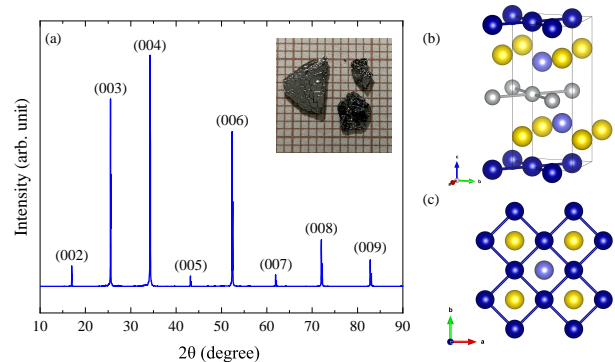


FIG. 1. (a) Single crystal XRD pattern of PrAgBi₂. Inset shows the optical image of single crystals (b) A schematic diagram of the crystal structure, with Pr atoms marked in yellow, Ag atoms in gray, and Bi1 and Bi2 in dark and light blue, respectively. (c) Bi square lattice seen along the c -axis.

self-consistent field calculations were completed using a $10 \times 10 \times 5$ k -point grid, while the Fermi surface was evaluated on a $51 \times 51 \times 31$ grid in a non-SCF run. The resulting FS and a summary of dHvA calculations are presented in the Supplemental Material.

III. RESULTS AND DISCUSSION

A. Crystal structure

The x-ray diffraction pattern obtained for a single crystal is presented in Fig 1(a). The compound crystallizes in a space group $P4/nmm$ (No. 129), adopting a layered tetragonal (ZrCuSi₂-type) structure commonly reported for 122 compounds. The observed XRD reflections match well with the expected (00 l) positions, which confirms that the c -axis is perpendicular to the flat plane of the crystal. LeBail analysis of the data collected for powder samples (see Supplemental Material [42]) leads to lattice parameters $a = 4.5078(2)$ Å and $c = 10.4632(7)$ Å, which falls in between the previously reported values for the related compounds LaAgBi₂ and SmAgBi₂ [27], as expected due to the lanthanide contraction effect. The crystal structure is presented schematically in Fig 1(b). It is composed of alternating layers of Bi⁻¹ square net and [AgBi]⁻² slabs, separated by Pr⁺³ ions. Fig 1(c) presents a closer look at the square Bi lattice viewed along the c -axis.

B. Crystalline electric field

Fig. 2(a) displays the temperature-dependent magnetic susceptibility ($\chi = M/H$) data measured at $\mu_0 H = 0.1$ T for different crystallographic orientations of the PrAgBi₂ single-crystal. Below 12 K, the $\chi(T)$ data exhibits a broad hump along $H \parallel c$, whereas susceptibility

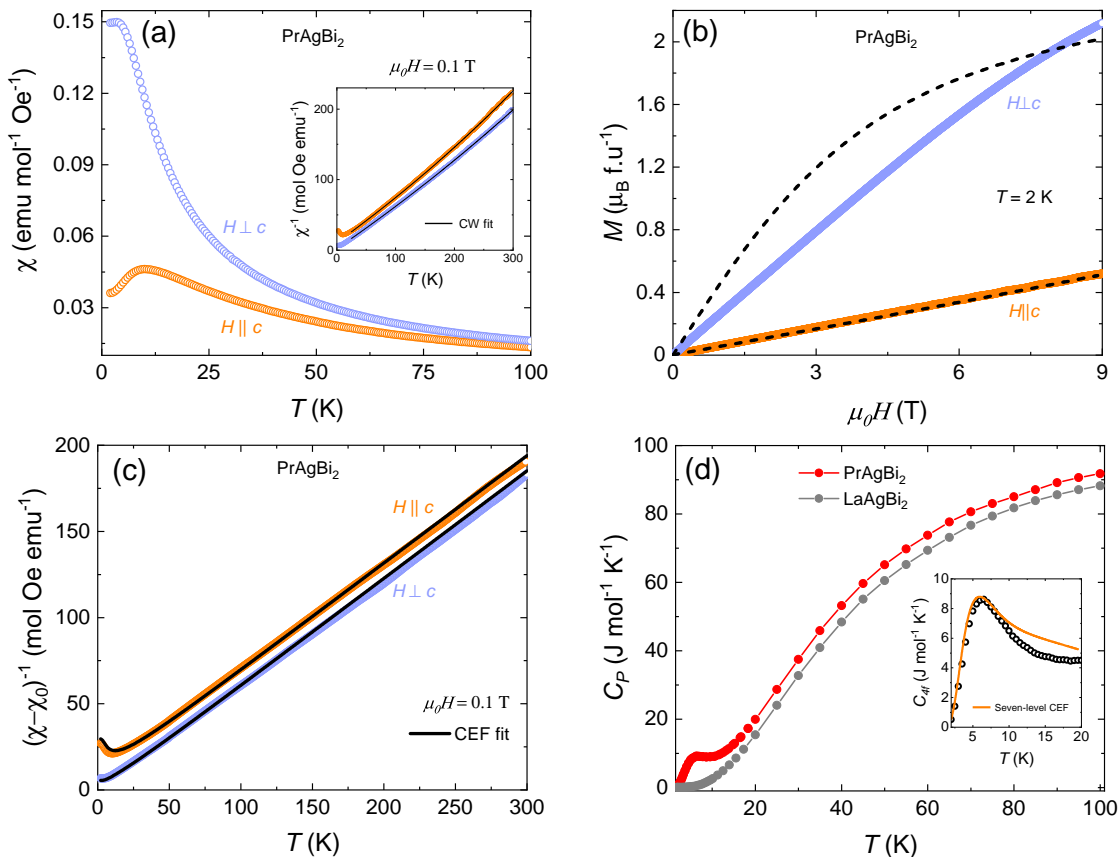


FIG. 2. (a) Temperature dependence of magnetic susceptibility of PrAgBi₂ along different crystallographic orientations measured at 0.1 T. The inset displays the inverse susceptibility as a function of temperature. The black line is the CW fit in the temperature range of 25–300 K. (b) Magnetic field-dependent isothermal magnetization measured at 2 K along two crystallographic orientations. Dotted lines are the calculated magnetization using CEF parameters. (c) The CEF fitting to the magnetic susceptibility for $H \parallel c$ and $H \perp c$ in the temperature range 2–300 K. (d) The temperature-dependent heat capacity of PrAgBi₂ and LaAgBi₂. The inset shows the f electron contribution to the heat capacity in the temperature range of 2–20 K. The solid orange line is the Schottky contribution to the heat capacity calculated using CEF energy levels.

TABLE I. The estimated χ_0 , μ_{eff} , and Θ_P from the modified Curie-Weiss fit to the inverse magnetic susceptibility data for different crystallographic directions of PrAgBi₂.

	$H \parallel c$	$H \perp c$
χ_0 (10^{-4} emu/mol)	-7.86(3)	-3.83(3)
μ_{eff} (μ_B)	3.7(1)	3.7(1)
Θ_P (K)	-18.2(1)	-3.8(1)

saturates along $H \perp c$ at low temperatures. Such temperature dependence of magnetic susceptibility indicates the existence of the CEF effect rather than a magnetic phase transition in PrAgBi₂ [27, 28]. High-temperature susceptibility data follows modified Curie-Weiss (CW)

behavior

$$\chi(T) = \chi_0 + \frac{C}{T - \Theta_P}. \quad (1)$$

The inset of Fig. 2(a) illustrates the fitting of the inverse magnetic susceptibility to the modified CW equation in the temperature range of 25–300 K for $H \parallel c$ and $H \perp c$. The obtained temperature independent susceptibility (χ_0), effective moment (μ_{eff}) and CW temperature (Θ_P) are presented in Table I. The so-obtained Θ_P is comparable to the previous report, and the estimated effective moment is close to the theoretical value ($3.58 \mu_B$) for Pr³⁺ free-ions [27]. The negative value of Θ_P indicates the predominance of antiferromagnetic interaction in the paramagnetic states. The isothermal magnetization $M(H)$ measured at 2 K for $H \parallel c$ and $H \perp c$ is shown in Fig. 2(b). Magnetization in PrAgBi₂ increases monotonically with increasing applied magnetic field without saturating even up to 9 T, as observed in several Pr-based CEF systems like PrAgSb₂, PrNi₂Cd₂₀, and PrPd₂Cd₂₀ [28, 43].

TABLE II. The estimated CEF parameters such as energy levels and the corresponding wave functions of PrAgBi₂

CEF parameters									
B_2^0 (K)	B_4^0 (K)	B_4^4 (K)	B_6^0 (K)	B_6^4 (K)	λ_i (mol/emu)				
0.91	0.0045	0.14	0	0.0054	$\lambda_z = 2.7; \lambda_{x,y} = -1.7$				
Energy levels and wave functions									
E (K)	+4⟩	+3⟩	+2⟩	+1⟩	0⟩	-1⟩	-2⟩	-3⟩	-4⟩
95.8	0.601	0	0	0	0.527	0	0	0	0.601
69.2	$-1/\sqrt{2}$	0	0	0	0	0	0	0	$1/\sqrt{2}$
54.6	0	0.577	0	0.409	0	0.409	0	0.577	0
54.6	0	-0.577	0	0.409	0	-0.409	0	0.577	0
41.3	0	0	$-1/\sqrt{2}$	0	0	0	$-1/\sqrt{2}$	0	0
18.1	0	0	$-1/\sqrt{2}$	0	0	0	$1/\sqrt{2}$	0	0
12.9	0	0.409	0	0.577	0	-0.577	0	-0.409	0
12.9	0	0.409	0	-0.577	0	-0.577	0	0.409	0
0.0	0.373	0	0	0	-0.849	0	0	0	0.373

To address the anomaly in the low-temperature magnetic susceptibility data, we have analyzed the $\chi(T)$ data using a multilevel CEF scheme. PrAgBi₂ crystallizes in a tetragonal structure with point symmetry D_{4h} , thus for Pr³⁺ ($J = 4$) total multiplet $(2J+1) = 9$, splits into two doublets and five singlets [44, 45]. For such a system, the CEF Hamiltonian is defined as

$$\mathcal{H}_{CEF} = B_2^0 O_2^0 + B_4^0 O_4^0 + B_4^4 O_4^4 + B_6^0 O_6^0 + B_6^4 O_6^4 \quad (2)$$

where B_l^m and O_l^m are the CEF parameters and the Stevens operators, respectively [46, 47]. As per the CEF scheme, the temperature-dependent magnetic susceptibility is expressed as follows:

$$\chi_{CEF}^i = \frac{N_A (g_J \mu_B)^2}{Z} \left[\sum_n \beta |\langle n | J_i | n \rangle|^2 e^{-\beta E_n} + \sum_{n \neq m} |\langle m | J_i | n \rangle|^2 \frac{e^{-\beta E_n} - e^{-\beta E_m}}{E_m - E_n} \right] \quad (3)$$

Here N_A and g_J are the Avogadro constant and Landé factor, respectively. $Z = \sum_n e^{-\beta E_n}$, where $\beta = 1/k_B T$ and $|n\rangle$ is the n th eigenfunction with eigenvalue E_n . J_i ($i = x, y,$ and z) is the component of angular momentum [48]. The first term of the Eq. 3 represents the Curie contribution to the susceptibility, and the second is the Van Vleck susceptibility. The overall magnetic susceptibility,

including molecular field (λ_i) contribution, is calculated as

$$(\chi_i - \chi_0)^{-1} = (\chi_{CEF}^i)^{-1} - \lambda_i. \quad (4)$$

The calculated temperature-dependent inverse magnetic susceptibilities data for different crystallographic directions are in good agreement with the experimentally observed data, as shown in Fig. 2(c). The estimated CEF parameters and corresponding energy levels and wave functions from the calculation are presented in Table II. To ensure the consistency of the analysis, a CEF parameter B_2^0 is directly calculated from the Curie-Weiss temperatures for different crystal orientations using the formula [49]

$$\Theta_P^{ab} - \Theta_P^c = \frac{3}{10} B_2^0 (2J-1)(2J+3), \quad (5)$$

which yields $B_2^0 = 0.62$, close to the value estimated from the CEF model fit.

Additionally, we use the following Hamiltonian to estimate the isothermal magnetization data using the CEF model

$$\mathcal{H} = \mathcal{H}_{CEF} - g_j \mu_B J_i (H + \lambda_i M_i), \quad (6)$$

where \mathcal{H}_{CEF} is the CEF Hamiltonian mentioned in Eq. 2. The second and third terms of the above expression

represent the Zeeman and molecular field contributions to the total Hamiltonian, respectively. The magnetization (M_i) along different crystallographic directions can be calculated using the expression

$$M_i = \frac{gJ\mu_B}{Z} \sum_n |\langle n | J_i | n \rangle| e^{-\beta E_n}. \quad (7)$$

The eigenvalue and associated eigenfunction of the above expression are derived by diagonalizing the entire Hamiltonian described in Eq. 6. The calculated magnetization at 2 K using CEF parameters for $H \parallel c$ and $H \perp c$ is approximately replicates the experimental data as displayed in Fig. 2(b). However, this computation precisely recognizes the anisotropy of magnetization.

Fig. 2(d) shows the temperature-dependent heat capacity $C_P(T)$ for PrAgBi₂ and the nonmagnetic reference LaAgBi₂. The heat capacity data exhibits a rather broad anomaly around 7 K, which may be associated with the Schottky-type anomaly resulting from the splitting of energy levels due to CEF effect, as seen in the similar compound PrAgSb₂ [28]. The Schottky contribution to the heat capacity for the multilevel system can be expressed as:

$$C_{Sch}(T) = \left(\frac{R}{T^2} \right) \left[\sum_i g_i e^{-\Delta_i/T} \sum_i g_i \Delta_i^2 e^{-\Delta_i/T} - \left(\sum_i g_i \Delta_i e^{-\Delta_i/T} \right)^2 \right] \left(\sum_i g_i e^{-\Delta_i/T} \right)^{-2}, \quad (8)$$

where R is the molar gas constant and g_i is the degeneracy of the i th state with Δ_i energy gap splitting [50]. The estimated Schottky heat capacity using the same CEF energy levels as given in Table II fairly reproduces the $4f$ contribution to the specific heat (C_{4f}), calculated using the formula $C_{4f} = C_P(\text{PrAgBi}_2) - C_P(\text{LaAgBi}_2)$, as displayed in the inset of Fig. 2(d). This finding further validates the estimated CEF energy levels in PrAgBi₂.

C. Quantum oscillations

The dHvA quantum oscillations are observed in the field-dependent isothermal magnetization (M) data along $H \parallel c$ in the high field region and temperature up to 14 K, as depicted in Fig. 3(a). The oscillatory component of the magnetization ΔM is extracted by subtracting a polynomial background resulting in prominent oscillations, as shown in Fig. 3(b). The oscillation amplitude of the magnetization can be expressed using the Lifshitz-Kosevich (LK) formula [51]

$$\Delta M \propto -B^{1/2} R_T R_D \sin \left[2\pi \left(\frac{F}{B} - \gamma - \delta \right) \right] \quad (9)$$

where R_T is the thermal damping factor, which is defined as $R_T = \frac{\alpha T \mu / B}{\sinh(\alpha T \mu / B)}$, $\alpha = 14.69$ T/K and $\mu = m^*/m_e$. m^* is the effective cyclotron mass. The term $R_D = \exp(\alpha T_D \mu / B)$ stands for the Dingle damping factor with Dingle temperature T_D , which is connected to the quantum scattering lifetime (τ_q) through the expression $\tau_q = \hbar / (2\pi k_B T_D)$. The phase factor γ is directly related to the Berry phase (Φ_B) through the expression $\gamma = 1/2 - \Phi_B / 2\pi$. The factor δ represents the additional phase shift, which is 0 for 2D systems and $\pm 1/8$ for 3D systems [52]. Fig. 3(b) shows the fast Fourier transform (FFT) spectra of dHvA oscillations data at various temperatures, indicating a fundamental frequency of $F = 77$ T. The effective cyclotron mass is calculated by fitting the temperature-dependent FFT amplitudes to R_T , which yields $m^* \simeq 0.11 m_e$ as shown in Fig. 3(d). The obtained effective mass is comparable to several isostructural compounds such as LaAgBi₂ [29], GdAgSb₂ [32], SmAgSb₂ [33], and AMnBi₂ [5, 6]. The orthogonal cross-sectional area (A) corresponding to the frequency F can be calculated using the Onsager equation $F = (\hbar/2\pi e)A$, resulting in $A = 0.73$ nm⁻². Assuming circular Fermi-surface cross-section Fermi wave vector (k_F) and velocity (v_F) are estimated to be 0.48 nm⁻¹ and 0.51×10^6 ms⁻², respectively, using the expression $k_F = \sqrt{2eF/\hbar}$ and $v_F = \hbar k_F / m^*$. Further Dingle temperature is calculated from the field-dependent oscillatory part of the LK equation as presented in the inset of Fig. 3(d). The obtained $T_D = 3$ K and corresponding quantum scattering lifetime $\tau_Q = 4.05 \times 10^{-13}$ s and quantum mobility $\mu_Q = e\tau_Q/m^* = 6534$ cm²V⁻¹s⁻¹. All the estimated parameters are summarized in Table III.

To get an estimation of the Berry phase, dHvA oscillations data is fitted to the LK equation as shown in Fig. 3(e). To reduce the dependency of too many fitting parameters, we use the effective mass and Dingle temperature that we obtained from previous analysis. The estimated value of the Berry phase is 0.84π . Further, the Berry phase is also estimated from the Landau level (LL) fan diagram to get a more reliable value. The LL index is assigned as $n+1/4$ and $n-1/4$ against the peaks and valleys, respectively, for the ΔM data at 2 K, as shown in Fig. 3(f). The slope of the linear fit of the LL indices indicates the oscillation frequency equal to 75.9 T, which is very close to that obtained from the FFT, validating the constructed LL fan diagram. The intercept $n_0 = 0.40$, and the corresponding Berry phase can be calculated using the expression $\Phi_B = 2\pi(n_0 + \delta)$ [53–55]. For $\delta = 0$, $\Phi_B = 0.8\pi$, which is comparable to that estimated from the LK fit. The obtained values of Φ_B taking $\delta = \pm 1/8$ are 1.05π and 0.55π , respectively. The nonzero Berry phase, which serves as an indicator of the topological nature of a system, implies the possible existence of Dirac fermions in PrAgBi₂ [5, 6, 33].

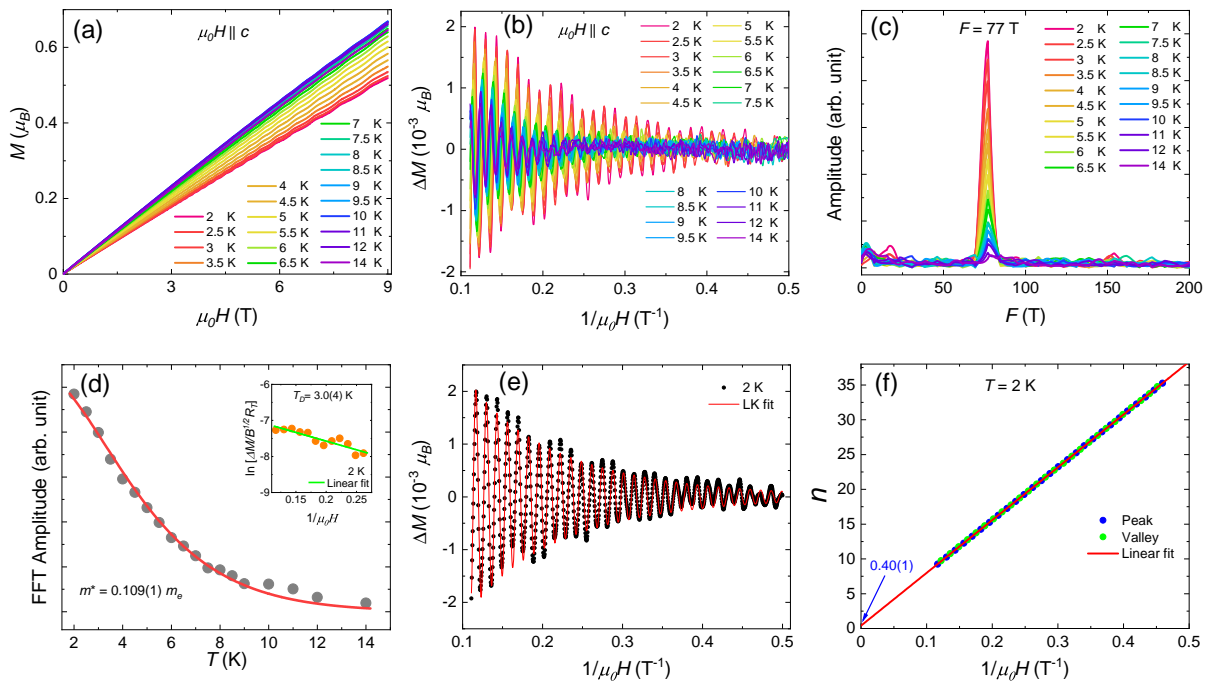


FIG. 3. (a) Field-dependent magnetization for various temperatures along $H||c$. (b) The oscillatory component of the magnetization data as a function of $1/\mu_0 H$. (c) The fast Fourier transform spectra of dHvA oscillations data for various temperatures. (d) Temperature dependence of FFT amplitude. The solid red line is a fit to the temperature-dependent term R_T of the LK equation. The inset shows the Dingle plot. (e) Fitting of dHvA data with the LK equation at 2 K. (f) LL fan diagram: The peaks $(n+1/4)$ and valleys $(n-1/4)$ are assigned blue and green dots, respectively.

TABLE III. Parameters obtained from the dHvA quantum oscillations.

$F(T)$	$A(\text{nm}^{-2})$	$k_f(\text{nm}^{-1})$	$v_f(10^6 \text{ms}^{-1})$	m^*/m_e	$T_D(K)$	$\tau_Q(10^{-13}\text{s})$	$\mu_Q(\text{cm}^2\text{V}^{-1}\text{s}^{-1})$	$\Phi_B(\delta=0)$
77	0.73	0.48	0.51	0.11	3	4.05	6534	0.8π

D. Linear magnetoresistance

The electrical resistivity $\rho(T)$ of single-crystalline PrAgBi₂ as a function of temperature for current flowing in the ab -plane is shown in Fig. 4(a). The electrical resistivity decreases monotonically with decreasing temperature, showing metallic behavior. No pronounced anomaly is seen; however, around 10 K, a hump-like feature is observed in the $\rho(T)$ data, consistent with the previous report [27]. The broad peak in $\rho(T)$ could be associated with CEF effect seen in the temperature-dependent magnetic susceptibility and heat capacity data. At 2 K, a significant decrease in the resistivity is observed, resulting in a large residual resistivity ratio (RRR). The electrical transport measurements were carried out on four single crystals obtained from different crystal growths. The RRR value ranges from 50 to 67, indicating that the as-grown crystals are of excellent quality and the results are reproducible. The inset of Fig. 4(a) shows the $\rho(T)$

in the temperature range of 2–20 K under a few constant applied magnetic fields along the c -axis. The resistivity is enhanced significantly without changing its feature as the applied field increase, indicating large magnetoresistance in PrAgBi₂.

The field-dependent magnetoresistance measurements were conducted on four different crystals in the temperature range 2–20 K for $H||c$ direction and current in the ab -plane, as illustrated in Figs. 4(b)–4(e). Large, non-saturating linear MR is observed in all crystals. MR reaches 1060% at 2 K and 9 T in sample S1, whereas other samples display a relatively low MR. The crystal quality strongly influences the value of MR as observed in the case of LaAgBi₂ [56]. In addition, a slight misalignment of the sample plane with the applied magnetic field may also lead to variation in the MR, as the Fermi surface of these series of compounds is highly anisotropic [29]. Nevertheless, all crystals display a similar field and temperature dependence. The MR

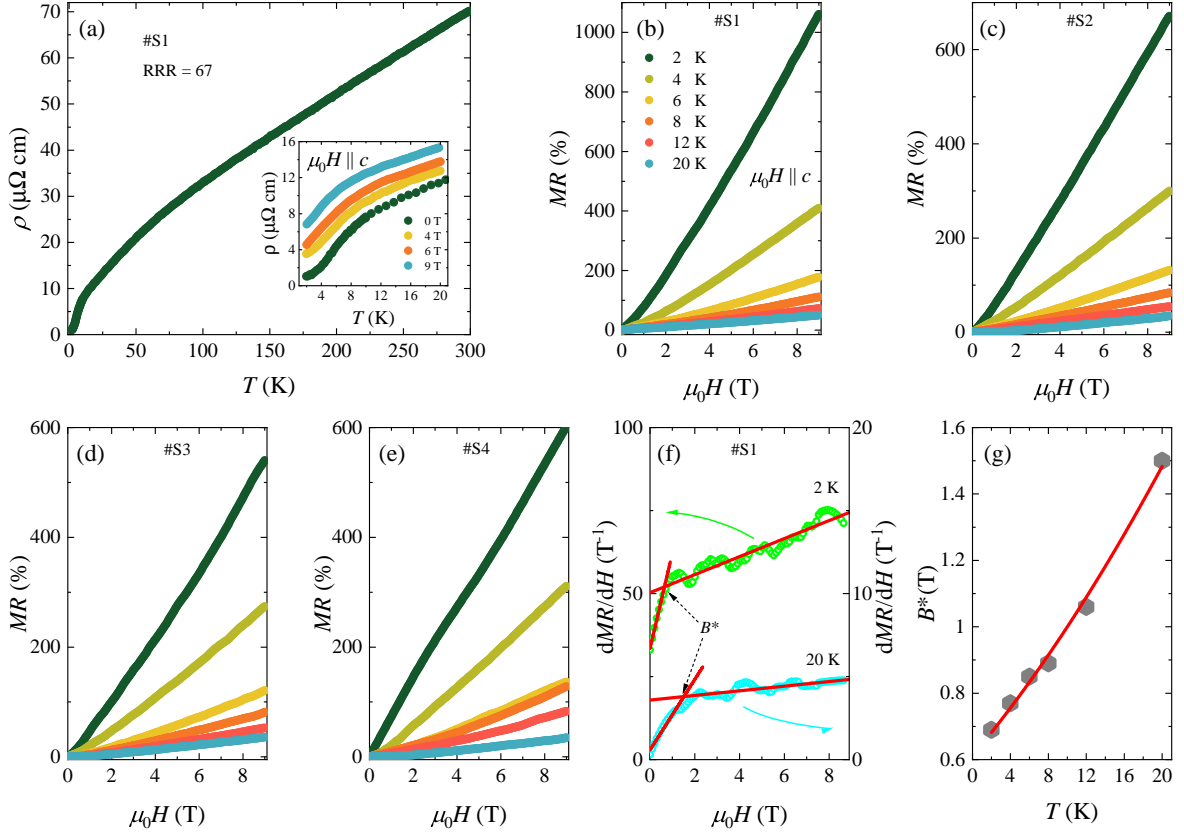


FIG. 4. (a) Electrical resistivity as a function of temperature in the absence of an external magnetic field. Inset shows the resistivity in the temperature range 2-20 K for the applied magnetic field $\mu_0 H = 0, 4, 6, 9$ T. (b)-(d) Field-dependent magnetoresistance measured up to 9 T on different single crystals at $T = 2, 4, 6, 8, 12,$ and 20 K. (e) Field-dependent magnetoresistance with respect to the applied field at 2 K and 20 K. (f) First-order derivative of magnetoresistance with respect to the applied field at 2 K and 20 K. (g) The estimated critical field as a function of temperature. The red line is the fitting of the data with the expression of $B^*(T)$ as described in the text.

shows a strong temperature dependence; as the temperature increases, the MR drops significantly. Besides the linear MR in the high field, PrAgBi_2 exhibits a semiclassical quadratic field dependency in the weak field regime. The quadratic nature becomes more pronounced at higher temperatures. The field-dependent MR at low temperatures in PrAgBi_2 manifests a significant deviation from semiclassical transport and a violation of Kohler's scaling (see SM [42]), implying the involvement of relativistic fermions, multiband, or quantum effects in magnetotransport [29, 30, 57–59]. Recently, linear and unsaturated MR has been observed in several quasi-2D system featuring a Dirac band dispersion, including BaFe_2As_2 [60], Bi/Sb square net LaAgBi_2 [29], LaAgSb_2 [30], and CaMnBi_2 [5, 61]. Such unusual MR in these compounds has been interpreted using Abrikosov's theorem of quantum limit, in which all the carriers (electrons or holes) in the Dirac states are confined to the zeroth Landau level. In such scenario, the Fermi energy E_F and thermal fluctuations $k_B T$ must be less than the energy level splitting between the zeroth and first LLs, denoted by $\Delta_{LL} = \pm v_F \sqrt{2\hbar e B}$. Dirac fermions have

a high Fermi velocity; thus, the splitting energy for relativistic fermions is much higher than that of conventional fermions in the parabolic bands, where LL splitting energy $\Delta = \hbar e B / m^*$. As a result, a quantum limit can be realized in moderately applied magnetic fields in topological materials [60, 62–64]. It can be anticipated that the Dirac-like dispersive band in PrAgBi_2 may lead to large, linear, and nonsaturating MR as observed in isostructural systems like LaAgBi_2 [29] and CaMnBi_2 [5]. Moreover, a crossover from the quadratic to linear dependence in MR is pointed out as the critical field B^* in the $\frac{d\text{MR}}{dH}$ vs. $\mu_0 H$ data as shown in Fig. 4(f). In the low-field region, the first derivative of MR follows linear dependence, reflecting semiclassical MR behavior. Whereas in the higher field it has a much-reduced slope, implying a dominating linear response with a small quadratic factor in the field-dependent MR. The temperature dependence of the critical field, as presented in Fig. 4(g), is well described by the expression $B^*(T) = \frac{1}{2e\hbar v_F^2} (E_F + k_B T)^2$ [5, 29, 60], where Fermi energy $E_F = 2.9$ meV and Fermi velocity $v_F = 0.64 \times 10^6$ ms $^{-1}$. This further indicates the influence

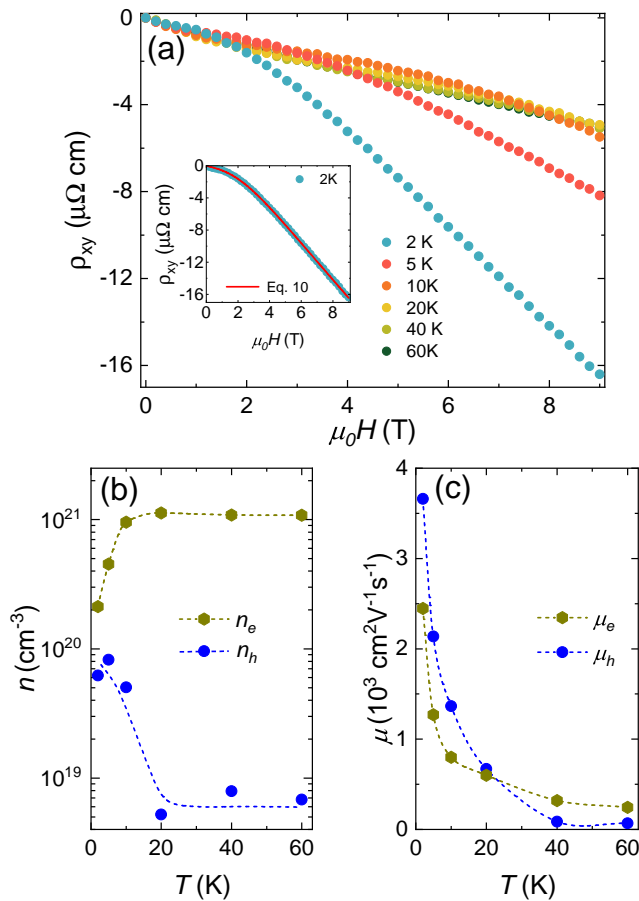


FIG. 5. (a) Hall resistivity as a function of magnetic field of PrAgBi₂ measured in the temperature range 2-60 K. The inset shows the Hall resistivity at 2K, fitted with the two-band model (Eq. 10). The temperature dependence of carrier concentrations (n_e & n_h) and mobilities (μ_e & μ_h) is shown in (b) and (c), respectively.

of Dirac fermions on the magnetotransport properties of PrAgBi₂, consistent with our band structure calculation discussed below.

E. Hall resistivity

The field dependence of Hall resistivity ρ_{xy} measured in the 2-60 K temperature range is presented in Fig. 5(a). Hall resistivity exhibits a negative slope and non-linear behavior at low temperatures; as the temperature increases, ρ_{xy} becomes linear. These observations suggest that the transport in PrAgBi₂ involves two types of carriers, with electrons being the predominant type. The semi-classical two-band model was used to estimate the concentrations and mobilities of the carriers, where Hall resistivity is defined as,

$$\rho_{xy} = \frac{\mu_0 H}{e} \frac{(n_h \mu_h^2 - n_e \mu_e^2) + (n_h - n_e) \mu_e^2 \mu_h^2 (\mu_0 H)^2}{(n_h \mu_h + n_e \mu_e)^2 + (n_h - n_e)^2 \mu_e^2 \mu_h^2 (\mu_0 H)^2}, \quad (10)$$

where, n_e and n_h (μ_e and μ_h) are the carrier concentration (mobility) of the electrons and holes, respectively. Figures. 5(c) and 5(d), depict the temperature variation of carrier concentrations and mobilities estimated by fitting Eq. 10 to the Hall resistivity data. At low temperatures, the estimated electron (hole) concentration $\sim 10^{20} \text{ cm}^{-3}$ ($\sim 10^{19} \text{ cm}^{-3}$) and the mobility $\sim 10^3 \text{ cm}^2 \text{ V}^{-1} \text{ s}^{-1}$ are comparable to several topological materials [30, 33, 65]. The electron concentration increases to $\sim 10^{21} \text{ cm}^{-3}$ as the temperature increases, whereas hole concentration decreases to $\sim 10^{18} \text{ cm}^{-3}$. A significant drop in mobility is observed in both cases as the temperature increases.

F. Electronic band structure

Fig. 6 presents the results of electronic structure calculations of PrAgBi₂. As expected, the band structure (Fig. 6(a)) is remarkably similar to the isoelectronic LaAgBi₂ [56] and LaAuBi₂ [66, 67]. The density of states at the Fermi level, $DOS(E_F)$, is mostly contributed by Bi $6p$ states as shown in Fig. 6(b). This suggests that the electronic properties of PrAgBi₂ derive from the square Bi⁻¹ network, in agreement with chemical bonding considerations [1, 25, 26]. The calculated Fermi surface (FS), shown in Fig. 6(d,e), consists of three branches (marked with green, yellow, and red). Two of the FS branches (marked in red and yellow) touch at a high symmetry line W spanning from the X point at the zone boundary to the R point at the zone edge, forming a Dirac point (DP) at $k \approx (0.0, 0.5, 0.279)$ in crystal coordinates (see Fig. 6(f-h)), protected by the non-symmorphic n glide symmetry operation. Band dispersions around the DP in the vicinity of E_F are plotted in Fig. 6(f). The calculated Fermi velocity in the vicinity of the DP are slightly above $0.5 \times 10^6 \text{ ms}^{-1}$ (Fig. 6(g)), in a reasonable agreement with the value estimated from the magnetoresistance analysis.

The calculation of the dHvA oscillation frequencies (see the SM[42]) indicates that the observed oscillation with frequency $F = 77 \text{ T}$ can be attributed to a set of orbits contained in the branch of the FS shown in green in Fig. 6 (d,e). This band has a nontrivial character, forming a Dirac point located at 0.41 eV below the E_F at the R point of the BZ [see Figs. 6(i-k)]. Such observation is consistent with the value of the Berry phase estimated from the dHvA oscillation data, which suggests the existence of Dirac fermions in PrAgBi₂.

The two bands marked in yellow and red in Fig. 6(a,f,i) have a linear dispersion around the E_F and their crossing lies very close to the Fermi level. In case of the remaining band, the Dirac point is located below the Fermi level and the dispersion relation is nonlinear around E_F . Thus the results of electronic structure calculations allow us to assume that linear MR and observed dHvA oscillations result from two separate parts of the Fermi surface - the former is associated with the Dirac bands crossing at the

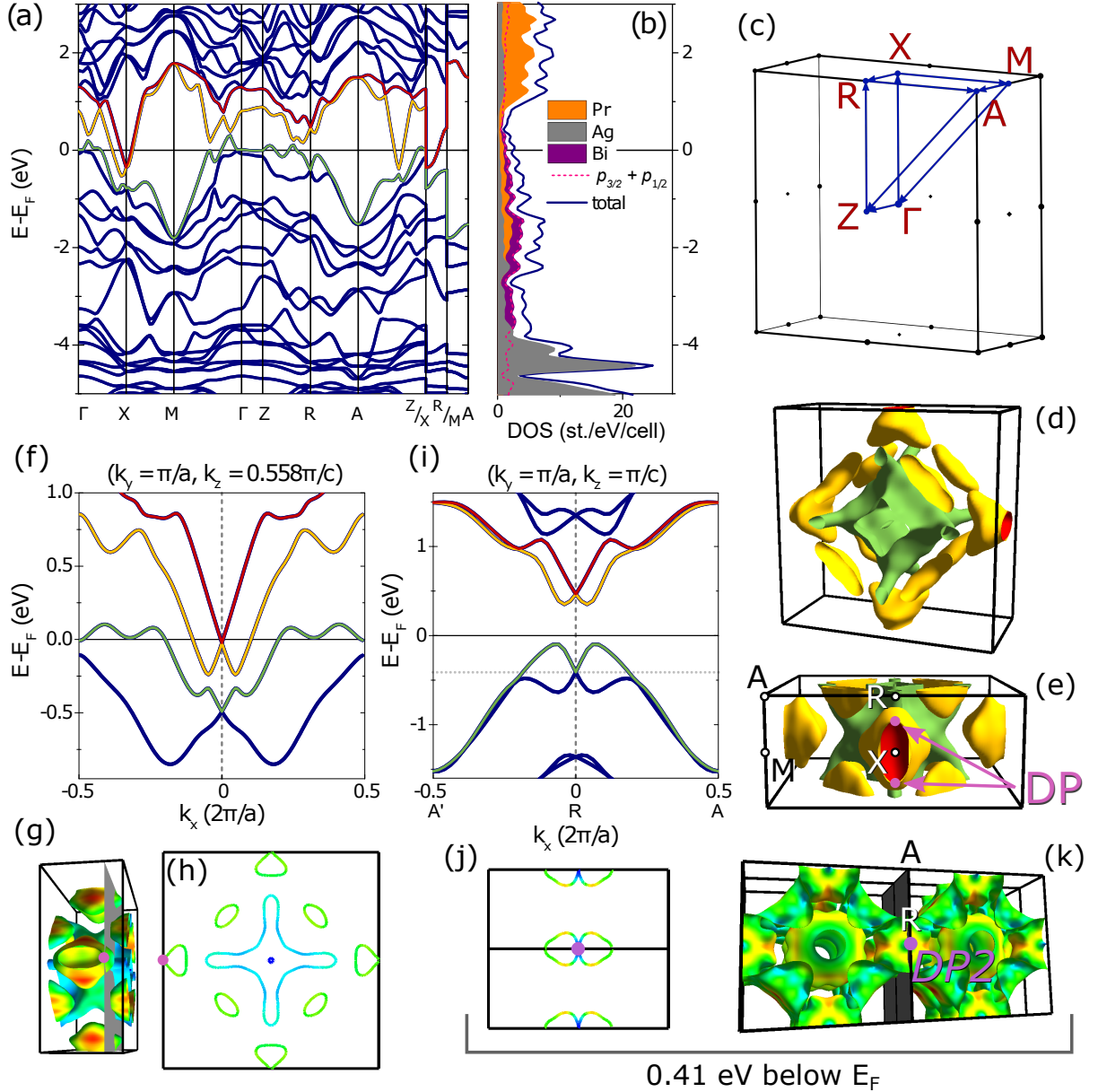


FIG. 6. Band structure (a) and density of states (b) of PrAgBi_2 . Three bands crossing the Fermi level are highlighted in green, yellow and red. (c) High symmetry points of the first Brillouin zone (BZ). Panels (d) and (e) present two projections of the calculated Fermi surface of PrAgBi_2 . Dirac points lying close to the Fermi level are labeled in pink, high-symmetry points - in black and white. Panel (f) shows the band dispersion around the Dirac point positioned at $k = (0.0, 0.5, 0.279)$ in crystal coordinates, which lies at the Fermi level. Panels (g) and (h) show two sections of the FS colored according to the modulus of the Fermi velocity. In panel (g) the section cuts through the Dirac point (one of the four DPs at the plane is highlighted in pink). Panel (i) shows the band dispersion along the $A'-R-A$ line. A symmetry protected crossing (DP2, purple) is found at the R point, 0.41 eV below the Fermi level. The band shown in green forms one of the branches of the Fermi surface, which is responsible for the observed dHvA oscillations (see SM [42]). Panels (j) and (k) show the Fermi surface for the Fermi energy shifted downwards by 0.41 eV, at which energy the second Dirac point (DP2) is found.

Fermi level at $k = (0.0, 0.5, 0.279)$, while the latter stems from tubular features of one of the FS branches (see the SM [42] Fig. S4), which forms a Dirac point at the R point of the BZ, positioned 0.41 eV below the Fermi level.

IV. CONCLUSION

In conclusion, we have carried out a systematic analysis of magnetic and magnetotransport properties, together with the band structure calculation of high-quality single

crystals of PrAgBi₂. The analysis of magnetization and heat capacity data confirms the crystalline electric field effect in the absence of any magnetic phase transition in PrAgBi₂. The ground-state energy level is determined to be divided into two doublets and five singlets. The de Haas-van Alphen quantum oscillations data shows a nonzero Berry phase and a very small cyclotron effective mass, indicating nontrivial topological state. A linear and unsaturated magnetoresistance in PrAgBi₂ is observed in the magnetotransport measurements. Interestingly, the field-dependent magnetoresistance data show a crossover from a weak-field quadratic dependency to a high-field linear dependence. The crossover critical field B^* exhibits a quadratic temperature dependence, implying the splitting of linear energy dispersion in PrAgBi₂. The band structure calculation reveals bands with linear

dispersion and a Dirac point located at the BZ boundary, which is likely responsible for the observed linear MR, while the dHvA oscillation was ascribed to particular nontrivial band that forms a protected crossing ca. 0.41 eV below the Fermi level. Therefore, our investigation indicates the existence of Dirac fermions in the quasi-two-dimensional CEF system PrAgBi₂.

V. ACKNOWLEDGMENT

Research performed at Gdansk Tech. was supported by the National Science Center (Poland), Project No. 2022/45/B/ST5/03916. S. M. thanks Daloo Ram for valuable discussions.

-
- [1] S. Klemenz, S. Lei, and L. M. Schoop, Topological semimetals in square-net materials, *Annual Review of Materials Research* **49**, 185 (2019).
- [2] S. L. Bud'ko, P. C. Canfield, C. H. Mielke, and A. H. Lacerda, Anisotropic magnetic properties of light rare-earth dantimonides, *Phys. Rev. B* **57**, 13624 (1998).
- [3] Q. Jiang, D. Wang, Z. Liu, Z. Jiang, H. Qian, X. Shen, A. Li, D. Shen, S. Qiao, and M. Ye, Topological surface states in superconducting CaBi₂, *Phys. Rev. B* **104**, 245112 (2021).
- [4] M. Sakano, K. Okawa, M. Kanou, H. Sanjo, T. Okuda, T. Sasagawa, and K. Ishizaka, Topologically protected surface states in a centrosymmetric superconductor β -PdBi₂, *Nature communications* **6**, 8595 (2015).
- [5] K. Wang, D. Graf, L. Wang, H. Lei, S. W. Tozer, and C. Petrovic, Two-dimensional Dirac fermions and quantum magnetoresistance in CaMnBi₂, *Phys. Rev. B* **85**, 041101 (2012).
- [6] J. Park, G. Lee, F. Wolff-Fabris, Y. Y. Koh, M. J. Eom, Y. K. Kim, M. A. Farhan, Y. J. Jo, C. Kim, J. H. Shim, and J. S. Kim, Anisotropic Dirac Fermions in a Bi Square Net of SrMnBi₂, *Phys. Rev. Lett.* **107**, 126402 (2011).
- [7] H. Masuda, H. Sakai, M. Tokunaga, Y. Yamasaki, A. Miyake, J. Shiogai, S. Nakamura, S. Awaji, A. Tsukazaki, H. Nakao, *et al.*, Quantum Hall effect in a bulk antiferromagnet EuMnBi₂ with magnetically confined two-dimensional Dirac fermions, *Science advances* **2**, e1501117 (2016).
- [8] M. J. Winiarski, B. Wiendlocha, S. Gołab, S. K. Kushwaha, P. Wiśniewski, D. Kaczorowski, J. D. Thompson, R. J. Cava, and T. Klimczuk, Superconductivity in CaBi₂, *Physical Chemistry Chemical Physics* **18**, 21737 (2016).
- [9] K. Górnicka, S. Gutowska, M. J. Winiarski, B. Wiendlocha, W. Xie, R. Cava, and T. Klimczuk, Superconductivity on a Bi square net in LiBi, *Chemistry of Materials* **32**, 3150 (2020).
- [10] S. K. Kushwaha, J. W. Krizan, J. Xiong, T. Klimczuk, Q. D. Gibson, T. Liang, N. P. Ong, and R. J. Cava, Superconducting properties and electronic structure of NaBi, *Journal of Physics: Condensed Matter* **26**, 212201 (2014).
- [11] J. B. He, Y. Fu, L. X. Zhao, H. Liang, D. Chen, Y. M. Leng, X. M. Wang, J. Li, S. Zhang, M. Q. Xue, C. H. Li, P. Zhang, Z. A. Ren, and G. F. Chen, Quasi-two-dimensional massless Dirac fermions in CaMnSb₂, *Phys. Rev. B* **95**, 045128 (2017).
- [12] H. Rong, L. Zhou, J. He, C. Song, J. Huang, C. Hu, Y. Xu, Y. Cai, H. Chen, C. Li, Q. Wang, L. Zhao, Z. Zhu, G. Liu, Z. Xu, G. Chen, H. Weng, and X. J. Zhou, Electronic structure examination of the topological properties of CaMnSb₂ by angle-resolved photoemission spectroscopy, *Phys. Rev. B* **103**, 245104 (2021).
- [13] B. Liu, Y. Fu, J. Cheng, W. Zhu, J. He, C. Liu, L. Li, and Y. Luo, Physical Properties of Antiferromagnetic Dirac Semimetal SrMnSb₂, *Journal of Superconductivity and Novel Magnetism* **35**, 3263 (2022).
- [14] S. Huang, J. Kim, W. A. Shelton, E. W. Plummer, and R. Jin, Nontrivial Berry phase in magnetic BaMnSb₂ semimetal, *Proceedings of the National Academy of Sciences* **114**, 6256 (2017).
- [15] H. Sakai, H. Fujimura, S. Sakuragi, M. Ochi, R. Kurihara, A. Miyake, M. Tokunaga, T. Kojima, D. Hashizume, T. Muro, K. Kuroda, T. Kondo, T. Kida, M. Hagiwara, K. Kuroki, M. Kondo, K. Tsuruda, H. Murakawa, and N. Hanasaki, Bulk quantum Hall effect of spin-valley coupled Dirac fermions in the polar antiferromagnet BaMnSb₂, *Phys. Rev. B* **101**, 081104 (2020).
- [16] L. Zhang, Z. Sun, A. Wang, Y. Xia, X. Mi, L. Zhang, M. He, Y. Chai, T. Wu, R. Wang, X. Zhou, and X. Chen, Strong coupling between magnetic order and band topology in the antiferromagnet EuMnSb₂, *Phys. Rev. B* **104**, 205108 (2021).
- [17] J. M. Wilde, S. X. M. Riberolles, A. Das, Y. Liu, T. W. Heitmann, X. Wang, W. E. Straszheim, S. L. Bud'ko, P. C. Canfield, A. Kreyssig, R. J. McQueeney, D. H. Ryan, and B. G. Ueland, Canted antiferromagnetic phases in the candidate layered Weyl material EuMnSb₂, *Phys. Rev. B* **106**, 024420 (2022).
- [18] Y. F. Guo, A. J. Princep, X. Zhang, P. Manuel, D. Khalyavin, I. I. Mazin, Y. G. Shi, and A. T. Boothroyd, Coupling of magnetic order to planar Bi electrons in the anisotropic Dirac metals AMnBi₂ (A = Sr, Ca), *Phys. Rev. B* **90**, 075120 (2014).

- [19] Y. Feng, Z. Wang, C. Chen, Y. Shi, Z. Xie, H. Yi, A. Liang, S. He, J. He, Y. Peng, *et al.*, Strong anisotropy of Dirac cones in SrMnBi₂ and CaMnBi₂ revealed by angle-resolved photoemission spectroscopy, *Scientific reports* **4**, 5385 (2014).
- [20] A. Zhang, C. Liu, C. Yi, G. Zhao, T.-l. Xia, J. Ji, Y. Shi, R. Yu, X. Wang, C. Chen, *et al.*, Interplay of Dirac electrons and magnetism in CaMnBi₂ and SrMnBi₂, *Nature communications* **7**, 13833 (2016).
- [21] G. Lee, M. A. Farhan, J. S. Kim, and J. H. Shim, Anisotropic Dirac electronic structures of AMnBi₂ ($A = \text{Sr, Ca}$), *Phys. Rev. B* **87**, 245104 (2013).
- [22] L. Li, K. Wang, D. Graf, L. Wang, A. Wang, and C. Petrovic, Electron-hole asymmetry, Dirac fermions, and quantum magnetoresistance in BaMnBi₂, *Phys. Rev. B* **93**, 115141 (2016).
- [23] H. Chen, L. Li, Q. Zhu, J. Yang, B. Chen, Q. Mao, J. Du, H. Wang, and M. Fang, Pressure induced superconductivity in the antiferromagnetic Dirac material BaMnBi₂, *Scientific Reports* **7**, 1634 (2017).
- [24] A. F. May, M. A. McGuire, and B. C. Sales, Effect of Eu magnetism on the electronic properties of the candidate Dirac material EuMnBi₂, *Phys. Rev. B* **90**, 075109 (2014).
- [25] S. Klemenz, A. K. Hay, S. M. L. Teicher, A. Topp, J. Cano, and L. M. Schoop, The Role of Delocalized Chemical Bonding in Square-Net-Based Topological Semimetals, *Journal of the American Chemical Society* **142**, 6350 (2020), publisher: American Chemical Society.
- [26] J. F. Khoury and L. M. Schoop, Chemical bonds in topological materials, *Trends in Chemistry* **3**, 700 (2021).
- [27] C. Petrovic, S. Bud'ko, J. Strand, and P. Canfield, Anisotropic properties of rare earth silver dibismites, *Journal of Magnetism and Magnetic Materials* **261**, 210 (2003).
- [28] K. Myers, S. Bud'ko, I. Fisher, Z. Islam, H. Kleinke, A. Lacerda, and P. Canfield, Systematic study of anisotropic transport and magnetic properties of RAgSb₂ ($R = \text{Y, La-Nd, Sm, Gd-Tm}$), *Journal of Magnetism and Magnetic Materials* **205**, 27 (1999).
- [29] K. Wang, D. Graf, and C. Petrovic, Quasi-two-dimensional Dirac fermions and quantum magnetoresistance in LaAgBi₂, *Phys. Rev. B* **87**, 235101 (2013).
- [30] K. Wang and C. Petrovic, Multiband effects and possible Dirac states in LaAgSb₂, *Phys. Rev. B* **86**, 155213 (2012).
- [31] X. Shi, P. Richard, K. Wang, M. Liu, C. E. Matt, N. Xu, R. S. Dhaka, Z. Ristic, T. Qian, Y.-F. Yang, C. Petrovic, M. Shi, and H. Ding, Observation of Dirac-like band dispersion in LaAgSb₂, *Phys. Rev. B* **93**, 081105 (2016).
- [32] S. Roy, R. Singha, R. Alam, and P. Mandal, Anisotropic transport properties and high-mobility of charge carriers of antiferromagnetic GdAgSb₂, *Journal of Physics: Condensed Matter* **35**, 425701 (2023).
- [33] J. Yuan, X.-B. Shi, H. Du, T. Li, C.-Y. Xi, X. Wang, W. Xia, B.-T. Wang, R.-D. Zhong, and Y.-F. Guo, Two-dimensional Sb net generated nontrivial topological states in SmAgSb₂ probed by quantum oscillations, *Chinese Physics B* **33**, 077102 (2024).
- [34] P. Giannozzi, S. Baroni, N. Bonini, M. Calandra, R. Car, C. Cavazzoni, D. Ceresoli, Chiarotti, and *et al.*, QUANTUM ESPRESSO: a modular and open-source software project for quantum simulations of materials, *Journal of Physics: Condensed Matter* **21**, 395502 (2009).
- [35] P. Giannozzi, O. Baseggio, P. Bonfà, D. Brunato, R. Car, I. Carnimeo, C. Cavazzoni, S. de Gironcoli, and *et al.*, Quantum ESPRESSO toward the exascale, *The Journal of Chemical Physics* **152**, 154105 (2020).
- [36] P. Giannozzi, O. Andreussi, T. Brumme, O. Bunau, M. B. Nardelli, M. Calandra, R. Car, C. Cavazzoni, D. Ceresoli, Cococcioni, and *et al.*, Advanced capabilities for materials modelling with Quantum ESPRESSO, *Journal of Physics: Condensed Matter* **29**, 465901 (2017).
- [37] J. P. Perdew, K. Burke, and M. Ernzerhof, Generalized Gradient Approximation Made Simple, *Physical Review Letters* **77**, 3865 (1996).
- [38] P. E. Blöchl, Projector augmented-wave method, *Physical Review B* **50**, 17953 (1994).
- [39] A. Dal Corso, Pseudopotentials periodic table: From H to Pu, *Computational Materials Science* **95**, 337 (2014).
- [40] M. Kawamura, FermiSurfer: Fermi-surface viewer providing multiple representation schemes, *Computer Physics Communications* **239**, 197 (2019).
- [41] P. Rourke and S. Julian, Numerical extraction of de Haas-van Alphen frequencies from calculated band energies, *Computer Physics Communications* **183**, 324 (2012).
- [42] See Supplemental Material at Phys. Rev. B for powder XRD data, EDS data, Kohler's plots and calculation of dHvA oscillations.
- [43] D. Yazici, T. Yanagisawa, B. D. White, and M. B. Maple, Nonmagnetic ground state in the cubic compounds PrNi₂Cd₂₀ and PrPd₂Cd₂₀, *Phys. Rev. B* **91**, 115136 (2015).
- [44] U. Walter, Treating crystal field parameters in lower than cubic symmetries, *Journal of Physics and Chemistry of Solids* **45**, 401 (1984).
- [45] D. Ram, S. Malick, Z. Hossain, and D. Kaczorowski, Magnetic, thermodynamic, and magnetotransport properties of CeGaGe and PrGaGe single crystals, *Phys. Rev. B* **108**, 024428 (2023).
- [46] K. W. H. Stevens, Matrix elements and operator equivalents connected with the magnetic properties of rare earth ions, *Proceedings of the Physical Society. Section A* **65**, 209 (1952).
- [47] M. Hutchings, Point-charge calculations of energy levels of magnetic ions in crystalline electric fields, *Solid State Physics Solid State Physics*, **16**, 227 (1964).
- [48] J. Banda, B. K. Rai, H. Rosner, E. Morosan, C. Geibel, and M. Brando, Crystalline electric field of Ce in trigonal symmetry: CeIr₃Ge₇ as a model case, *Phys. Rev. B* **98**, 195120 (2018).
- [49] Y.-L. Wang, Crystal-field effects of paramagnetic Curie temperature, *Physics Letters A* **35**, 383 (1971).
- [50] E. S. R. Gopal, *Specific heats at low temperatures* (Plenum, New York, 1966).
- [51] D. Shoenberg, *Magnetic oscillations in metals* (Cambridge university press, 2009).
- [52] J. Hu, Z. Tang, J. Liu, X. Liu, Y. Zhu, D. Graf, K. Myhro, S. Tran, C. N. Lau, J. Wei, and Z. Mao, Evidence of Topological Nodal-Line Fermions in ZrSiSe and ZrSiTe, *Phys. Rev. Lett.* **117**, 016602 (2016).
- [53] W. Xia, X. Shi, Y. Wang, W. Ge, H. Su, Q. Wang, X. Wang, N. Yu, Z. Zou, Y. Hao, W. Zhao, and Y. Guo, The de Haas-van Alphen quantum oscillations in a three-dimensional Dirac semimetal TiSb₂, *Applied Physics Letters* **116**, 142103 (2020).

- [54] X. Han, H. Pi, D. Yan, R. Zhang, Y. Li, X. Wang, Z. Dun, Z. Wang, H. L. Feng, Q. Wu, and Y. Shi, Quantum oscillations and transport evidence of topological bands in La_3MgBi_5 single crystals, *Phys. Rev. B* **108**, 075157 (2023).
- [55] Y. Zhu, J. Hu, D. Graf, X. Gui, W. Xie, and Z. Mao, Quasi-two-dimensional relativistic fermions probed by de Haas–van Alphen quantum oscillations in LuSn_2 , *Phys. Rev. B* **103**, 125109 (2021).
- [56] M. Murase and T. Sasagawa, Large Magnetoresistance and Dirac Line Node in LaAgBi_2 , *Journal of the Physical Society of Japan* **89**, 055003 (2020).
- [57] A. B. Pippard, *Magnetoresistance in metals*, Vol. 2 (Cambridge university press, 1989).
- [58] M. Kohler, Zur magnetischen Widerstandsänderung reiner Metalle, *Annalen der Physik* **424**, 211 (1938).
- [59] J. Xu, F. Han, T.-T. Wang, L. R. Thoutam, S. E. Pate, M. Li, X. Zhang, Y.-L. Wang, R. Fotovat, U. Welp, X. Zhou, W.-K. Kwok, D. Y. Chung, M. G. Kanatzidis, and Z.-L. Xiao, Extended Kohler’s Rule of Magnetoresistance, *Phys. Rev. X* **11**, 041029 (2021).
- [60] K. K. Huynh, Y. Tanabe, and K. Tanigaki, Both Electron and Hole Dirac Cone States in $\text{Ba}(\text{FeAs})_2$ Confirmed by Magnetoresistance, *Phys. Rev. Lett.* **106**, 217004 (2011).
- [61] J. B. He, D. M. Wang, and G. F. Chen, Giant magnetoresistance in layered manganese pnictide CaMnBi_2 , *Applied Physics Letters* **100**, 112405 (2012).
- [62] A. A. Abrikosov, Quantum magnetoresistance, *Phys. Rev. B* **58**, 2788 (1998).
- [63] A. H. Castro Neto, F. Guinea, N. M. R. Peres, K. S. Novoselov, and A. K. Geim, The electronic properties of graphene, *Rev. Mod. Phys.* **81**, 109 (2009).
- [64] J. Hu, S.-Y. Xu, N. Ni, and Z. Mao, Transport of topological semimetals, *Annual Review of Materials Research* **49**, 207 (2019).
- [65] Y.-Y. Wang, S. Xu, L.-L. Sun, and T.-L. Xia, Quantum oscillations and coherent interlayer transport in a new topological Dirac semimetal candidate YbMnSb_2 , *Phys. Rev. Mater.* **2**, 021201 (2018).
- [66] E. M. Seibel, W. Xie, Q. D. Gibson, and R. J. Cava, Structure and magnetic properties of the REAuBi_2 ($\text{RE}=\text{La-Nd, Sm}$) phases, *Journal of Solid State Chemistry* **230**, 318 (2015).
- [67] X. Yu, W. He, T. Yang, X. Wu, F. Chen, W. Wu, Y. Bi, and C. He, First-principles study on structural, mechanical, and electronic properties of REAuBi_2 ($\text{RE} = \text{La-Pr, Sm}$) intermetallic compounds, *AIP Advances* **12**, 105103 (2022).